Experimental Eye Research 160 (2017) 85–95

Contents lists available at ScienceDirect

Experimental Eye Research

journal homepage: www.elsevier.com/locate/yexer

Whole-globe biomechanics using high-field MRI

Andrew P. Voorhees [a], Leon C. Ho [a, e], Ning-Jiun Jan [a, c], Huong Tran [a, c], Yolandi van der Merwe [a, c], Kevin Chan [a, b, c, d, f, **], Ian A. Sigal [a, b, c, d, *]

[a] UPMC Eye Center, Eye and Ear Institute, Ophthalmology and Visual Science Research Center, Department of Ophthalmology, University of Pittsburgh, Pittsburgh, PA, USA
[b] McGowan Institute for Regenerative Medicine, University of Pittsburgh, Pittsburgh, PA, USA
[c] Department of Bioengineering, University of Pittsburgh, Pittsburgh, PA, USA
[d] Louis J. Fox Center for Vision Restoration, University of Pittsburgh, Pittsburgh, PA, USA
[e] Department of Electrical and Electronic Engineering, The University of Hong Kong, Hong Kong, China
[f] New York University (NYU) Langone Eye Center, NYU Langone Medical Center, Department of Ophthalmology, NYU School of Medicine, New York, NY, United States

ARTICLE INFO

Article history:
Received 7 September 2016
Received in revised form
15 May 2017
Accepted in revised form 16 May 2017
Available online 17 May 2017

Keywords:
Lamina cribrosa
Optic nerve head
Biomechanics
Glaucoma
High-field MRI
IOP

ABSTRACT

The eye is a complex structure composed of several interconnected tissues acting together, across the whole globe, to resist deformation due to intraocular pressure (IOP). However, most work in the ocular biomechanics field only examines the response to IOP over smaller regions of the eye. We used high-field MRI to measure IOP induced ocular displacements and deformations over the whole globe. Seven sheep eyes were obtained from a local abattoir and imaged within 48 h using MRI at multiple levels of IOP. IOP was controlled with a gravity perfusion system and a cannula inserted into the anterior chamber. T2-weighted imaging was performed to the eyes serially at 0 mmHg, 10 mmHg, 20 mmHg and 40 mmHg of IOP using a 9.4 T MRI scanner. Manual morphometry was conducted using 3D visualization software to quantify IOP-induced effects at the globe scale (e.g. axial length and equatorial diameters) or optic nerve head scale (e.g. canal diameter, peripapillary sclera bowing). Measurement sensitivity analysis was conducted to determine measurement precision. High-field MRI revealed an outward bowing of the posterior sclera and anterior bulging of the cornea due to IOP elevation. Increments in IOP from 10 to 40 mmHg caused measurable increases in axial length in 6 of 7 eyes of 7.9 ± 5.7% (mean ± SD). Changes in equatorial diameter were minimal, 0.4 ± 1.2% between 10 and 40 mmHg, and in all cases less than the measurement sensitivity. The effects were nonlinear, with larger deformations at normal IOPs (10–20 mmHg) than at elevated IOPs (20–40 mmHg). IOP also caused measurable increases in the nasal-temporal scleral canal diameter of 13.4 ± 9.7% between 0 and 20 mmHg, but not in the superior-inferior diameter. This study demonstrates that high-field MRI can be used to visualize and measure simultaneously the effects of IOP over the whole globe, including the effects on axial length and equatorial diameter, posterior sclera displacement and bowing, and even changes in scleral canal diameter. The fact that the equatorial diameter did not change with IOP, in agreement with previous studies, indicates that a fixed boundary condition is a reasonable assumption for half globe inflation tests and computational models. Our results demonstrate the potential of high-field MRI to contribute to understanding ocular biomechanics, and specifically of the effects of IOP in large animal models.

1. Introduction

A comprehensive characterization of eye biomechanics is necessary to understand its physiology and to help develop better methods for diagnosis and treatment of disease (Ethier et al., 2004; Pijanka et al., 2013). The eye, however, is biomechanically complex, with several interconnected components. Forces acting on one part of the eye can lead to deformations in other parts. Some of these

* Corresponding author. Ocular Biomechanics Laboratory, Department of Ophthalmology, University of Pittsburgh School of Medicine, 203 Lothrop Street, Rm 930, Pittsburgh, PA 15213, United States.
** Corresponding author. NeuroImaging Laboratory, Department of Ophthalmology, University of Pittsburgh School of Medicine, 3025 East Carson Street, Rm 159, Pittsburgh, PA 15203, United States.
E-mail addresses: chuenwing.chan@fulbrightmail.org (K. Chan), Ian@ocularbiomechanics.com (I.A. Sigal).
URL: http://www.ocularbiomechanics.com

http://dx.doi.org/10.1016/j.exer.2017.05.004
0014-4835/

effects can even act across the globe. As an example, increased aqueous outflow resistance in the anterior pole can cause elevated intraocular pressure (IOP). Elevated IOP in turn is transmitted to the optic nerve head (ONH), increasing the risk of neural tissue damage and glaucoma. Thus, an understanding of biomechanics-related eye physiology and pathophysiology requires the ability to measure simultaneously, over the whole globe, the often minute displacements and deformations of the tissues of the eye, preferably non-invasively.

Currently, there are few methods for non-invasively measuring tissue deformation over the whole globe, which include ultrasound, optical coherence tomography (OCT), and computed tomography (CT), but they all have important limitations (Bajwa et al., 2015; Brown et al., 2016; Fortune, 2015). Ultrasound has excellent penetration depth allowing for quantitative biomechanical analysis of the sclera and cornea, but insufficient resolution to discern the fine structures of the optic nerve head (ONH) (He and Liu, 2009; Palko et al., 2016). OCT is fast and has high resolution capable of measuring lamina cribrosa (LC) deformation, but depth of field and penetration are problematic (Kostanyan et al., 2015; Sigal et al., 2014; Wang et al., 2015). Recently, the so-called whole-eye OCT devices have permitted simultaneous imaging of both anterior (cornea) and posterior segments (macula or ONH), but do not provide data elsewhere (Dai et al., 2012; Fan et al., 2015b). CT can produce very high resolution images, capturing structures of the LC, but due to limited soft tissue contrast, additional contrast agents, which may affect tissue mechanics, or very high energy systems are required (Campbell et al., 2015; Coudrillier et al., 2016). Further, those high energy systems cannot be used in-vivo due to radiation exposure and are not widely available.

MRI offers practically unlimited penetration depth for ocular imaging (Duong et al., 2008; Langner et al., 2010), and with improvements in MRI field strength it is now possible to obtain μm-resolution scans without contrast agents (Ho et al., 2014b, 2016). In fact, we recently demonstrated that MRI can be used to image the microstructure of the sclera and lamina cribrosa (Ho et al., 2014b). Although in vivo and clinical MRI may be limited clinically by long scan times and motion artifacts, it is well suited for ex vivo mechanics studies. Our goal in this study, was to demonstrate the capabilities of high-field MRI for quantifying ocular displacements and deformations caused by variations in IOP over the whole eye.

2. Methods

2.1. Tissue preparation

Seven ovine eyes from animals of similar age, between 1 and 2 years old, were obtained from a local abattoir. Eyes were cleaned, rinsed and stored in PBS at 4 °C prior to testing. All eyes were processed and imaged within 48 h of death. Eyes were cannulated through the anterior chamber to allow for control of IOP inside the MRI scanner. IOP was varied by changing the height of PBS in a gravity perfusion system as previously described (Ho et al., 2014b, 2016) and monitored by a pressure transducer designed for MRI applications with a sensitivity of 1 mmHg (BIOPAC Systems, Goleta, CA, USA). Eyes were suspended in hydrogel in an open container, as we have described previously, to prevent the application of external forces (Ho et al., 2016). The same eyes were scanned serially under increasing levels of IOP: 0 mmHg, 10 mmHg, 20 mmHg, or 40 mmHg. Eyes were allowed to equilibrate for 20 min after an IOP increase before scanning. An equilibration time of 20 min was chosen as we have previously demonstrated that only minimal tissue deformation occurs after 15 min of equilibration in topographic images of the vitreo-retinal interface (Sigal et al., 2005). The pressure transducer was used to verify that a constant pressure was applied at the desired level during each experimental session.

2.2. MRI

All scans were performed using a 9.4 T/31-cm Varian/Agilent horizontal MRI scanner (Varian/Agilent, Santa Clara, CA, USA). All scans were obtained using fast spin-echo T2-weighted imaging. MRI parameters were as follows: repetition time/echo time = 2300/27.8 ms, echo train length = 8, and number of averages = 4. In-plane field of view was 34 × 34 mm^2, matrix size was 256 × 256, and resolution was 133 × 133 μm^2. T2-weighted imaging was chosen as it provides high contrast between collagen-rich tissues (with short T2) and the aqueous and vitreous fluids (with long T2).

All eyes were scanned with slice thicknesses of 1000 μm, and three eyes were additionally scanned with slice thicknesses of 300 μm. The time between the start of a scan and the next change in IOP was approximately 1 h. Two eyes were oriented so that the in-plane field of view aligned with the sagittal plane, and five samples were oriented so that the in-plane field of view aligned with the axial plane.

2.3. Analysis

Traditional manual morphometry was conducted using Fiji (Schindelin et al., 2012) and the 3D image analysis software Avizo to measure eye dimensions (FEI Visualization Sciences Group, Hillsboro Oregon; Fig. 1). Careful attention was given during marking to identify appropriate corresponding points for measurement. Since the eyes were imaged in an open container and allowed to move

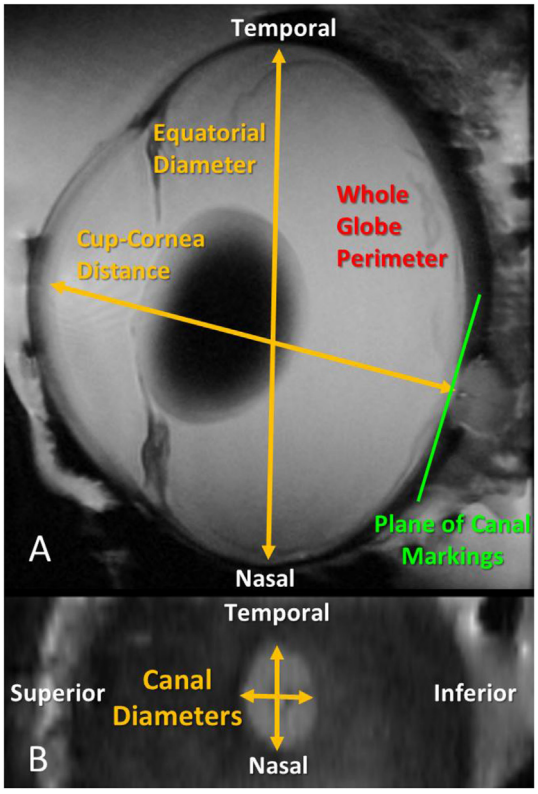

Fig. 1. Geometric parameters measured by high-field MRI in this study. A. On the global scale, cup-to-cornea distance (an approximation of axial length), equatorial diameter, and whole globe perimeter length, were measured. B. At the local level of the optic nerve head, the lengths of the scleral canal diameters were calculated. Canal dimensions were measured from coronal views of the optic nerve head.

freely within the soft gel, the eyes were free to displace and rotate as IOP changed. In preliminary tests we optimized eye placement and orientations for scanning so that the images of interest for morphometry would remain available at all pressures. This was facilitated by the use of the ObliqueSlice module in Avizo that allowed simultaneous comparison of multiple cross sections with arbitrary orientations by interpolating from the image intensity.

At the whole-globe level, measurements of equatorial diameter and cup to cornea distance (an approximation of axial length) were obtained through manual marking. Markings were made at sub-voxel resolution using 3D image interpolation functions available in Avizo. For one eye, the perimeter of the inner surface of the globe was manually delineated and the globe perimeter length was calculated for each pressure condition. Additionally, we examined the amount of posterior sclera bowing under the different levels of IOP. To demonstrate the potential of MRI for calculating local deformations, the dimensions of the scleral canal were measured under different levels of IOP to quantify canal expansion for three eyes. Anatomical landmarks including the position of the central retinal vessel and the vessel trunk as well as the shape of the canal were used to identify matching slices and corresponding locations. All markings and the determination of corresponding slices were verified by an expert in eye morphology (IAS) to ensure consistent markings. Whenever it was unclear if corresponding points could be confidently identified, the marks were removed from the analysis. Additionally, measurements of axial length in cases in which the low IOP caused anterior chamber collapse or an irregular cornea shape were not included in the analysis.

To establish the sensitivity of our MRI measurements, images from two eyes, one imaged with the superior-inferior plane aligned with the in-plane field and one imaged with the nasal-temporal plane aligned with the in-plane field were manually marked in triplicate. Sensitivity markings were made by a single marker (HT) on consecutive days. The standard deviation of each set of three markings was computed across each pressure. For estimates of canal diameter measurement sensitivity, standard deviations of both superior-inferior and nasal-temporal diameters were averaged. The mean of the standard deviations across all pressures and both eyes was then used to estimate the precision with which measurements could be made. When the magnitude of an IOP driven change was more than two times the average standard deviation across both sets of the triplicate markings, we were confident that change was not due to limitations on the resolution of the system and markings. Hence, we will define any change exceeding the two standard deviation threshold as “measureable.” Measurements are reported as mean ± standard deviation.

2.4. Sub-pixel resolution and non-linear interpolation

The measurements in this study were made utilizing sub-pixel resolution and non-linear interpolation. Our measurements use the information contained in the intensity gradient of an image to create a non-linear interpolation function which provides higher resolution than the original image. Done in this way, the edges can be identified at locations within a pixel rather than at pixel centroids. As a demonstration, we generated test images of circles varying in radius from 4 to 6 mm with an image pixel size of 500 × 500 μm using Matlab v2015b (Mathworks, Natick, MA; Fig. 2). The magnitude of the low-resolution image gradient was calculated and a cubic polynomial was fit to the gradient. The edge of the circle was then detected by selecting a contour using two different thresholds, for each image. The radii of the fitted circles were then calculated. While there was uncertainty in the absolute measurement of the radius partially due to the selection of the threshold, the difference in size between any two dimensions correlated very well with the actual difference in the image (Fig. 2E). In this example the uncertainty in the difference of measured radii was about 30 μm, less than 10% of the pixel size. For

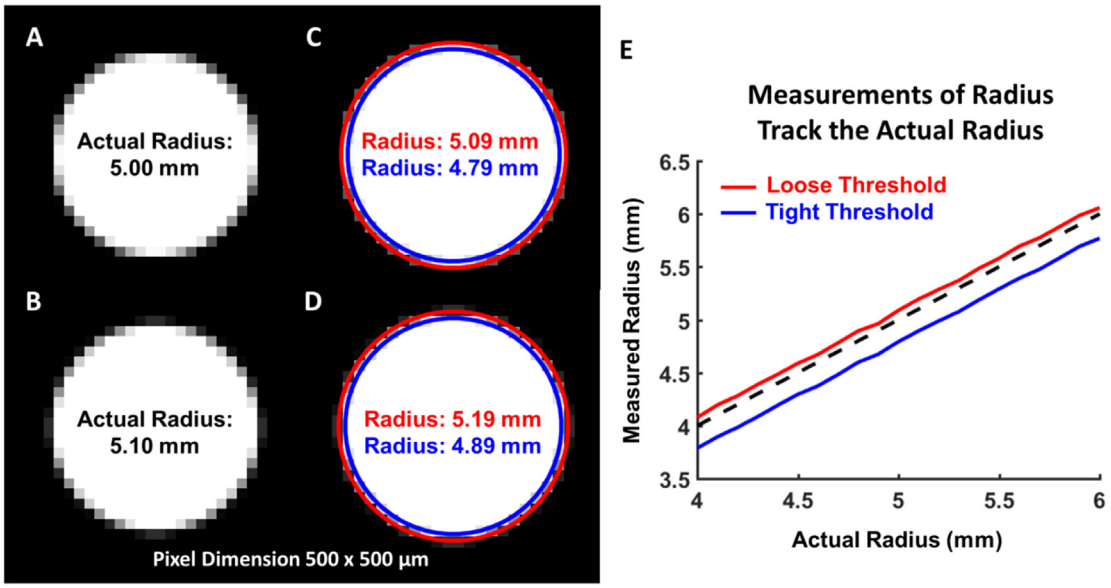

Fig. 2. An example of sub-pixel measurement using non-linear interpolation. A-B. Simulated low resolution images of two circles with a 0.1 mm difference in radius. Although, the images are similar, there are subtle differences in the gradient on the edge of the circle. C-D. A cubic polynomial was fit to the gradient of the image and edge contours were detected using two different thresholds, a loose threshold (Red) and a tight threshold (Blue). The radius calculated for each case depended upon the chosen threshold; however, the difference between two measurements made using the same threshold was accurate to 0.01 mm. Note that here we do not mean the difference between the measurements, which is 0.1 mm, but the accuracy of the difference, which is 0.01 mm. This is well below the pixel edge length of 0.5 mm. E. The difference between the actual radius and measured radius for each threshold was consistent as the actual radius was varied from 4 to 6 mm. Thus, while there is uncertainty in the absolute measurements which may be attributable to the choice of threshold, a consistent threshold will allow for accurate calculation of differences in size. (For interpretation of the references to colour in this figure legend, the reader is referred to the web version of this article.)

these reasons, we test changes in dimension rather than absolute dimensions.

3. Results

MRI scans produced images of the whole globe with clearly discernible cornea, equator and optic nerve head. Representative images from one eye are shown at IOPs of 0, 10, 20 and 40 mmHg in Fig. 3. Qualitatively, it is possible to notice the effects of increased IOP, such as a longer axial length with small changes in equatorial diameter, an outward bulging of the cornea and a posterior bowing of the sclera near the optic nerve head. Differences in eye geometry with IOP are more clearly visible using a green/yellow/red visualization of a representative eye at 10 mmHg and 40 mmHg, as in Fig. 4. The interior surface of a globe at the four different pressure conditions was delineated and registered (Fig. 5A, Supplementary Fig. 1). Posterior bowing of the sclera and outward bulging of the cornea are seen with increasing IOP, and the largest changes were seen between 10 and 20 mmHg. Globe perimeter increased by 0.4% between 0 and 10 mmHg, 3.5% from 10 to 20 mmHg, and a further 1.6% between 20 and 40 mmHg (Fig. 5B). This data bespeaks that corneoscleral shell mechanics are not linear with increasing IOP.

Mean standard deviation of the axial length for the eyes marked in triplicate, for sensitivity analysis, was 94 μm or 0.5% of the axial length (Fig. 6A). Measurable increases in axial length with IOP were found in 6 of the 7 eyes tested (Fig. 6B). Changes in axial length were non-linear, with a relative change in length between 10 and 20 mmHg of 6.0 ± 5.3% (1.1 ± 1.0 mm absolute change) and a change between 20 and 40 mmHg equal to 2.2 ± 1.9% (0.4 ± 0.4 mm absolute change). The mean standard deviation of equatorial diameter measurements was 178 μm or 0.7% of the equatorial length (Fig. 6C). No measurable changes in the equatorial diameter of the eyes were observed, 0.0 ± 0.9% (0.0 ± 0.2 mm absolute change) between IOPs of 10 and 20 mmHg, and 0.3 ± 1.3% (0.1 ± 0.3 mm

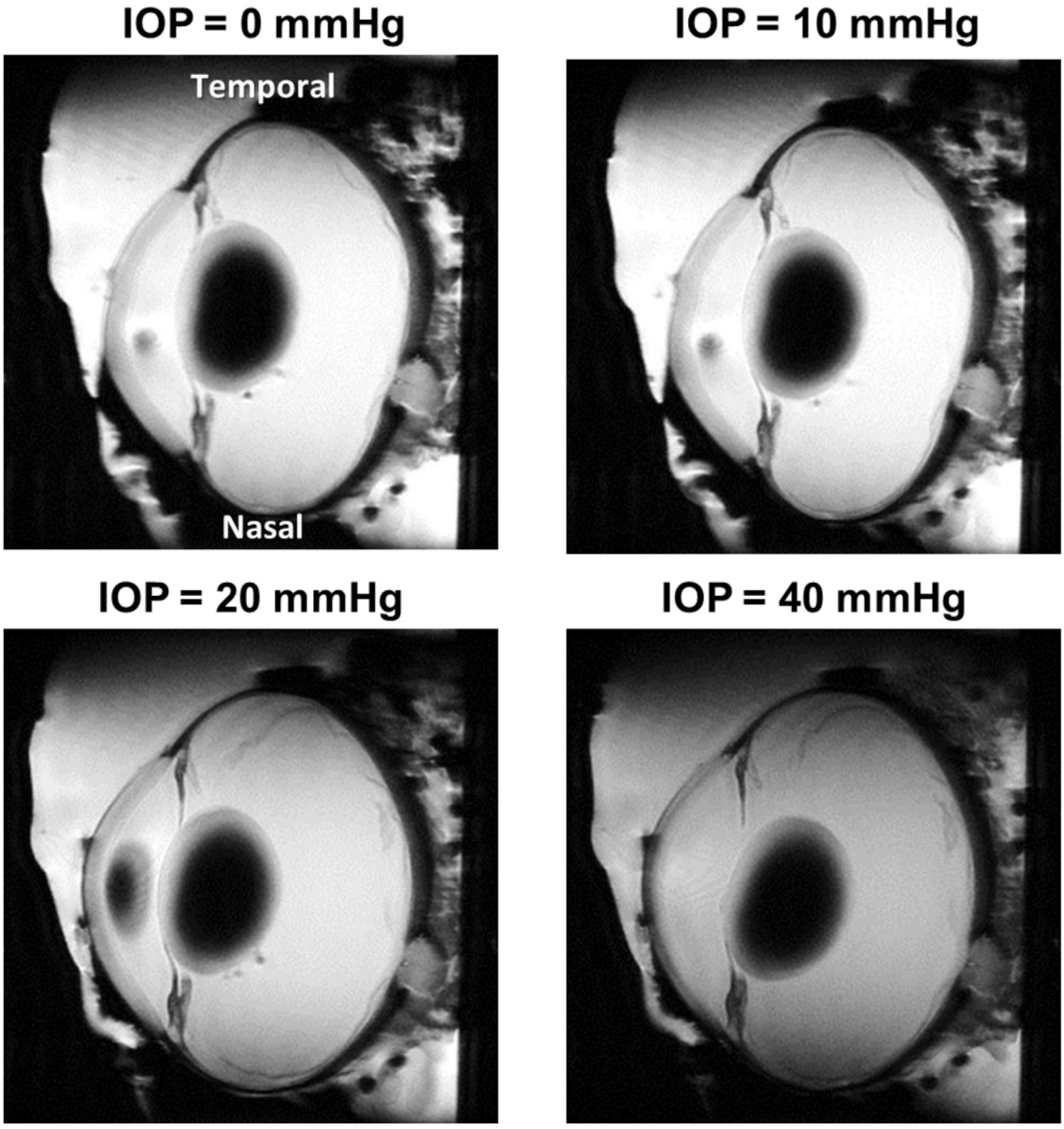

Fig. 3. Representative high-field MRI images of a sheep eye at controlled IOPs of 0, 10, 20 and 40 mmHg. Visually, an increase in axial length and globe cross-sectional area can be observed. The eye is oriented such that the nasal-temporal axis is vertical.

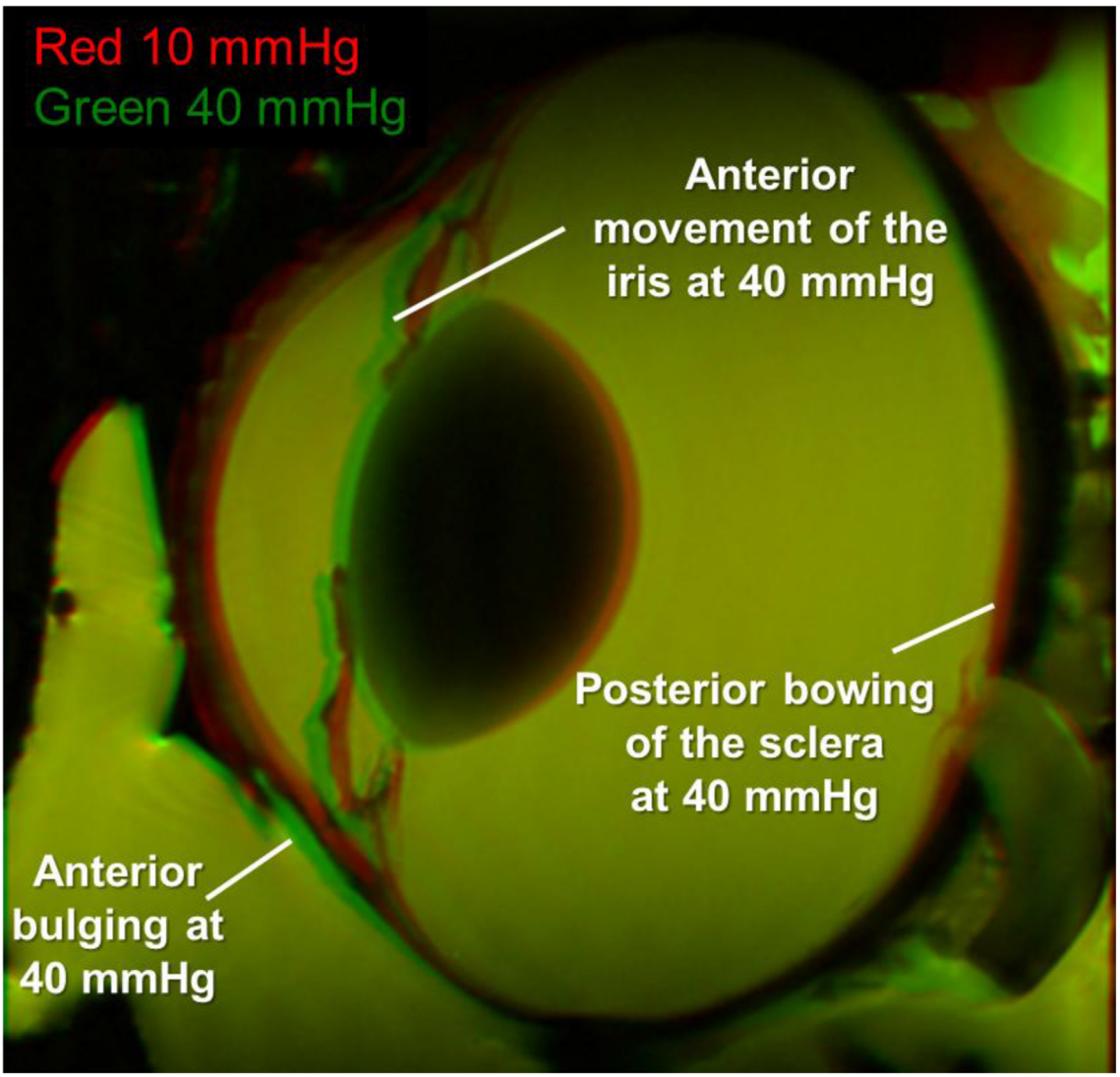

Fig. 4. Differences between an eye at 10 and 40 mmHg. The 10 mmHg image is colored in red and the 40 mmHg image is colored in green. At 40 mmHg the iris, cornea, and anterior sclera move anteriorly as indicated by the green regions noted on the figure. The posterior sclera bulges posteriorly at 40 mmHg as indicated by the red region corresponding to the 10 mmHg condition indicated on the figure. (For interpretation of the references to colour in this figure legend, the reader is referred to the web version of this article.)

absolute change) between IOPs of 20 and 40 mmHg (Fig. 6D).

To better visualize the outward bowing of the posterior sclera, both the inner and outer surfaces of the sclera as well as the anterior surface of the lamina cribrosa, and the outline of the optic nerve were delineated on an axial cross-section across all four pressures (Fig. 7). In one eye (Fig. 7A, Supplementary Fig. 2), the tracings highlight the minimal changes in the sclera between 0 and 10 mmHg, when the globe regains physiologic shape. This is followed by a substantial posterior bowing of the peripapillary sclera between 10 and 20 mmHg, with a lamina that is displaced posteriorly, without much deformation. Between 20 and 40 mmHg, scleral bowing ceases and the lamina becomes cupped within a distorted scleral canal. In another delineated eye (Fig. 7B, Supplementary Fig. 3) sclera bowing at elevated IOPs was seen, but without a discernible posterior deformation of the central lamina. The outward bulging of the optic nerve head is more clearly visible in Fig. 8.

Non-linear changes in scleral canal size were also observed, with a decrease in canal size occurring between 0 and 10 mmHg, a large increase occurring between 10 and 20 mmHg, and a smaller increase occurring between 20 and 40 mmHg (Fig. 9A). From the canal diameter measurement sensitivity analysis, we found an average standard deviation of the triplicate measurements equaling 30 μm or 1.3% of the average canal diameter (Fig. 9B) Measurements of the scleral canal diameters obtained from coronal views were calculated for the three eyes scanned with 300 μm slice thickness (Fig. 9C). Measurable scleral canal expansion due to IOP changes occurred in all three eyes. The nasal-temporal diameter of the scleral canal increased by 13.4 ± 9.7% (312 ± 190 μm absolute change) between 10 and 20 mmHg, and between 20 and 40 mmHg the change was 3.3 ± 0.9% (91 ± 24 μm absolute change). Changes in the superior-inferior canal diameter with IOP were smaller, and often negative, but did not meet the criteria for being measurable.

4. Discussion

We have demonstrated that high-field MRI is a viable tool for measuring whole eye deformations due to increases in IOP. Measurements of scleral canal diameter were obtained with 60 μm sensitivity while globe-scale measurements such as axial length

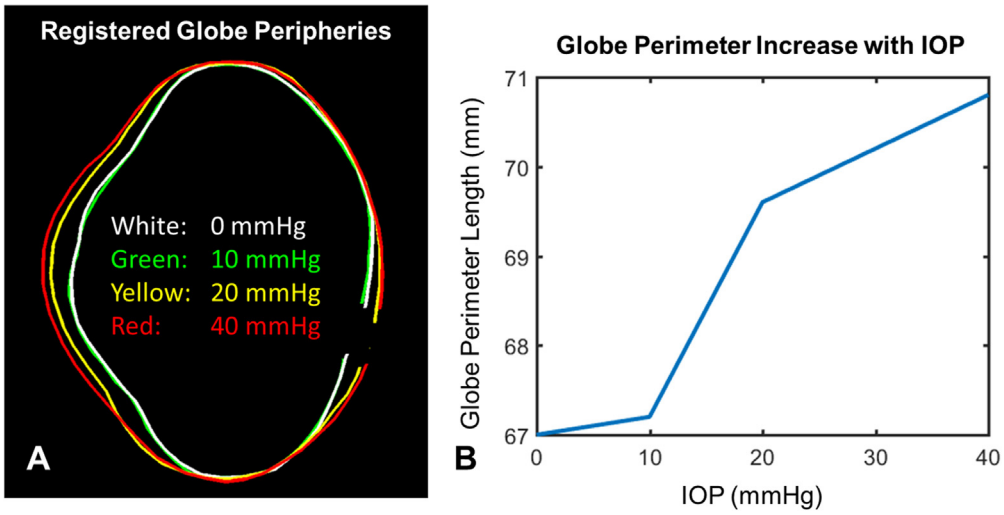

Fig. 5. Changes in globe perimeter. A. The peripheries of a globe are shown at different pressures. Delineations were registered along the globe equator. Delineation at the optic nerve head was done at the anterior lamina cribrosa surface. Clear corneal and posterior scleral bulging are observed at high pressures. Large changes are seen between 10 and 20 mmHg but not between 0 and 10 mmHg or between 20 and 40 mmHg. Delineations shown on the original images appear in Supplementary Fig. 1B. Globe perimeter increases non-linearly with increasing IOP, consistent with the non-linear mechanical properties of ocular tissues.

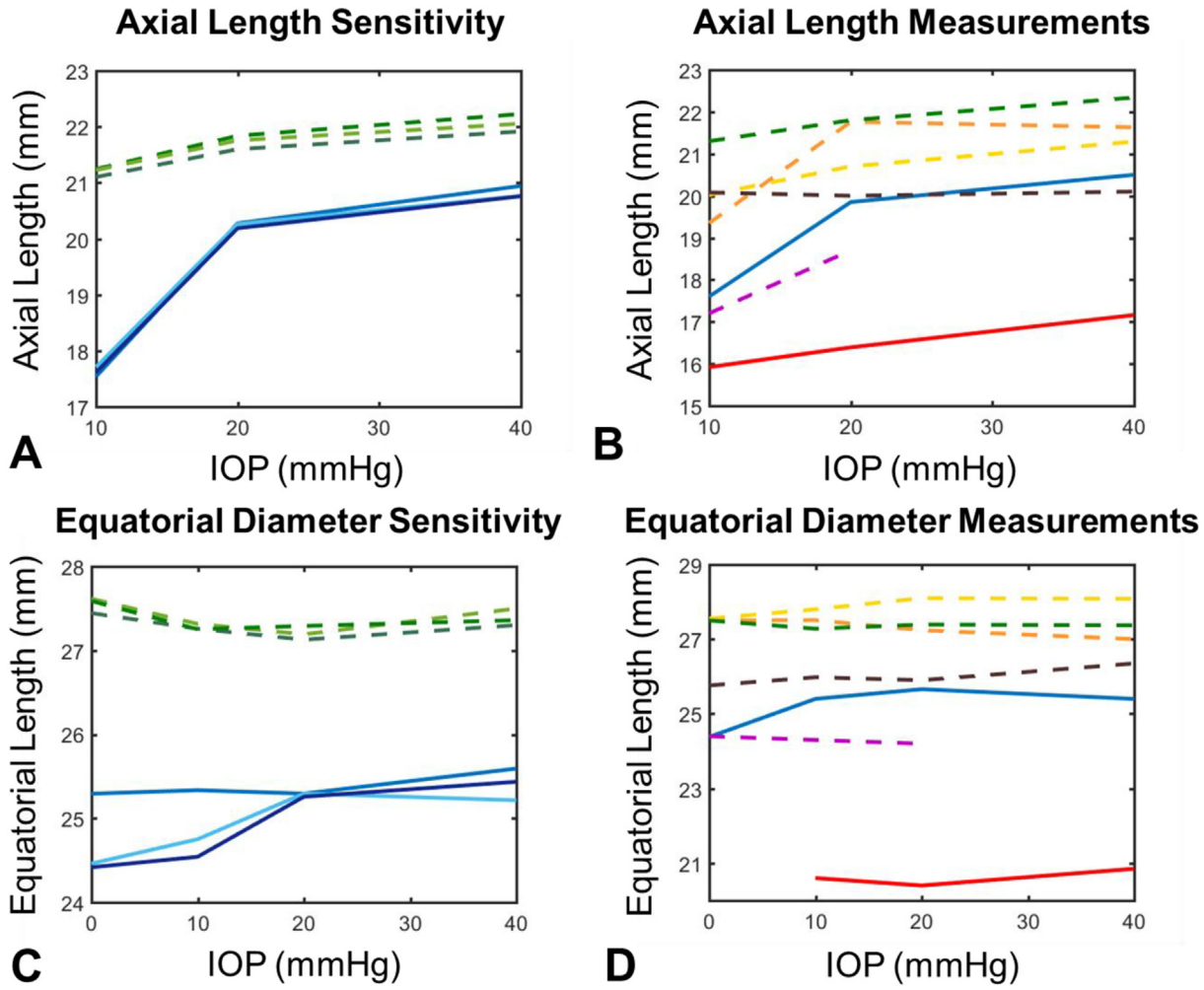

Fig. 6. Globe-level deformations of the eye. A. Axial length measurement sensitivity was computed by marking same images in triplicate. Differences between markings were small and mean standard deviation across all eyes and pressures was 94 μm. B. Axial length changes exceeded two times the average standard deviation from the sensitivity analysis in six of the seven eyes. Length changes were non-linear, with large deformations occurring between 10 and 20 mmHg and smaller changes between 20 and 40 mmHg. C. Equatorial diameter measurement sensitivity was also calculated and the average standard deviation across all eyes and pressures was 178 μm. D. No measureable changes in equatorial diameter, as defined by a change greater than twice the average standard deviation of the measurement sensitivity test, were observed. All colors correspond to same eyes across the four charts. Dashed lines represent measurements taken from images with best in-plane resolution in the sagittal plane and solid lines represent images with best in-plane resolution in the axial plane. Axial length was not measured at 0 mmHg as the cornea bowed inward at this sub-physiologic pressure. (For interpretation of the references to colour in this figure legend, the reader is referred to the web version of this article.)

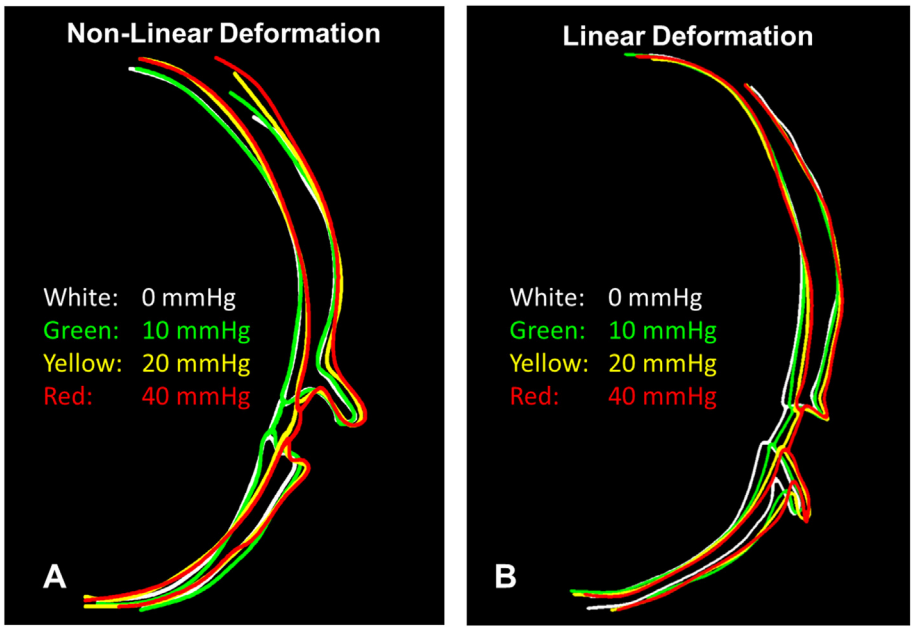

Fig. 7. Delineations of the posterior sclera and optic nerve head demonstrate scleral bowing and canal expansion with increasing IOP. To notice more clearly the outward bowing of the sclera and widening of the canal, the outlines were registered to one another in the peripheral sclera (notice the point where all lines cross) A. In one eye a non-linear deformation pattern was observed. Between 0 and 10 mmHg, little change was seen in the posterior sclera as the globe returned to its physiological shape. Between 10 and 20 mmHg the peripapillary sclera bowed outward and the lamina began to cup. Between 20 and 40 mmHg the sclera underwent only a small displacement, but noticeable deformation was seen in the canal and lamina surface. The delineations for this eye are shown on the original images in Supplementary Fig. 2B. In a second eye, the deformation pattern was much more linear with moderate scleral bowing observed at each pressure change and little deformation of the lamina cribrosa surface. The delineations for this eye are shown on the original images in Supplementary Fig. 3.

were obtained with 187 μm sensitivity. High-field MRI allowed us to observe complex, non-linear deformations of the eye with excellent detail and field of view.

Within our images, it is exciting to observe the non-linear behavior of the eye with increasing IOP. This non-linearity in the response to IOP is largely due to the mechanics of the collagen fibers within the ocular tissues of the sclera and cornea, a result of their microstructure (Jan et al., 2015; Sigal and Ethier, 2009). Much effort within the ocular biomechanics community has gone into measuring the non-linear material properties of the eye in order to better characterize how various parts of the eye, particularly the optic nerve head and lamina cribrosa, deform both under small deviations from physiological IOP and large deviations (Coudrillier et al., 2013; Girard et al., 2009; Grytz et al., 2014).

Another finding of our study was that the deformation of the scleral canal was highly anisotropic and quite large in the nasal-temporal direction, with the change in diameter exceeding 300 μm between 10 and 20 mmHg. To our knowledge there are no reported measurements of canal diameter change in sheep. Measurements in human and monkey have been done, but the findings of these studies have been quite varied (Albon et al., 2000; Bellezza et al., 2003a, 2003b; Strouthidis et al., 2011; Yan et al., 1994). Bellezza et al. measured the canal diameter in normal monkey eyes immersion fixed at an IOP of 0 mmHg and pressure fixed at an IOP of 10 mmHg and found differences in the superior-inferior diameter between the two conditions averaging 244 μm at the plane of the anterior laminar insertion (Bellezza et al., 2003a). In monkeys and humans, the long axis of the canal is in the superior-inferior direction while in sheep, the long axis is in the nasal-temporal direction. Albon et al. found that the change in axis length of the scleral canal in human eyes, was highly anisotropic and that the difference in axis length between 11 and 22 mmHg for eyes under 70 years old was around 6% (Albon et al., 2000). This is about half of the change we saw in the nasal-temporal direction for sheep between 10 and 20 mmHg, 13.6%. Other studies of scleral canal diameter and area change have reported negligible changes with increasing IOP (Bellezza et al., 2003b; Strouthidis et al., 2011; Yan et al., 1994) indicating that there may be very large individual variation. As a whole, our study demonstrates that high-field MRI is an important imaging tool available for whole-globe ocular biomechanics studies and could potentially be used to determine the non-linear material properties across the globe through inverse finite element modeling.

Another potential use of whole-globe high-field MRI imaging that may be of interest to the mechanics community is the determination of appropriate boundary conditions for excised tissue or partial globe mechanical tests and simulations. A common technique in the study of the ONH is to clamp the equatorial sclera and inflate the posterior half of the globe (Coudrillier et al., 2013, 2015). It is worried that this clamping may create an artificial constraint on the sclera and that these tests do not truly capture the in situ environment (Whitford et al., 2016). We found almost no change in equatorial diameter with IOP in sheep eyes. This is in agreement with the results of Sawada who found no change in rabbit eyes equatorial diameter due to a drop in pressure to sub-physiologic levels (Sawada et al., 2002). This indicates that a clamped boundary condition may be a reasonable assumption.

Multiple studies have looked at cornea properties to see if they can find associations with properties of the back of the eye (e.g. cornea and lamina thickness) (Jonas and Holbach, 2005), or with susceptibility to disease (cornea thickness and hysteresis vs. glaucoma progression) (Deol et al., 2015; Medeiros et al., 2013). We have demonstrated that we can detect not only the front and back of the eye simultaneously, but the side as well. This opens up the possibility of new studies on potential associations between ocular properties and disease. Further, whole-globe high-field MRI studies may improve our understanding of the influence of cornea and sclera thickness and stiffness on measurements of IOP which is

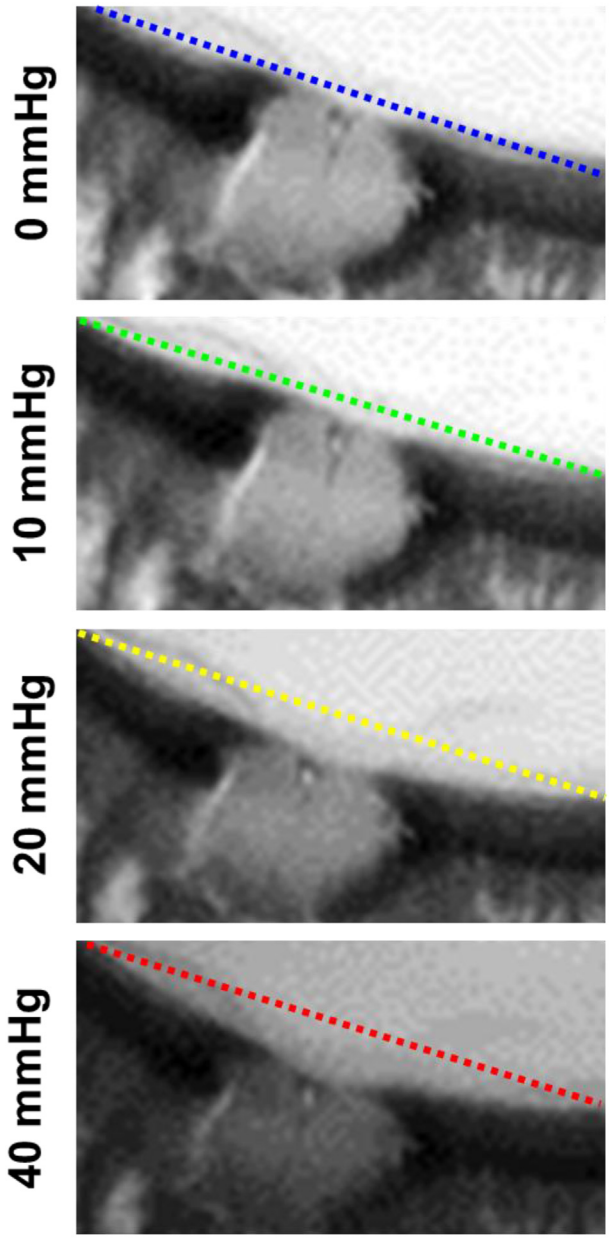

Fig. 8. Detailed view of axial cross sections through the optic nerve head and peripapillary sclera showing outward bowing of the sclera with increased IOP. Straight lines connecting the most distal sclera in the images are overlaid to help notice the deformations. Note also the detail and substantial deformations of structures posterior to the sclera, typically hidden from OCT due to shadowing.

known to confound the associations with disease in these studies.

In addition to MRI, there are several other imaging modalities available for studying ocular biomechanics. OCT has become a widely adopted clinical tool for imaging both the cornea, retina, and sclera with micron level resolution capable of measuring small deformations within these tissues (Kostanyan et al., 2015; Sigal et al., 2014; Strouthidis et al., 2011; Tran et al., 2015). However, OCT relies on light penetration and reflection and as such cannot image tissues deep into the sclera or optic nerve and can only image limited fields of view. “Whole eye” OCT systems which use a dual band, dual focus system to simultaneously image the cornea, anterior segment, and posterior pole have been developed to address the limited field of view (Dai et al., 2012; Fan et al., 2015b). However, this technique still doesn't capture the equatorial sclera limiting its potential for studying whole eye biomechanics.

Ultrasound relies on the reflection of soundwaves rather than light waves, and hence has better tissue depth penetration than OCT. In fact, ultrasonagraphy has been used to visualize the whole eye, however it is limited by rather low resolution and low contrast (Kilker et al., 2014; Lorente-Ramos et al., 2012). High frequency ultrasound designed for small animal imaging has recently been used to measure deformations of the porcine sclera in an ex vivo inflation test, however high frequency ultrasound lacks the depth penetration to study a whole eye from a large animal (Cruz Perez et al., 2016).

Computed tomography (CT) can be used to image the whole eye in vivo, however traditional approaches lack soft tissue contrast and may not be a good a choice for observing small deformations such as those that would occur with IOP (Malhotra et al., 2011). Recently, Micro-CT methods have been developed which offer improved resolution, however these methods require the use of alcohol based contrast agents which alter the hydration status of the eye and a fine beam radiation source such as a synchrotron (Campbell et al., 2015; Coudrillier et al., 2016; Hann et al., 2011).

While we believe high-field MRI has many advantages over these other methods: high soft tissue contrast without added contrast agents, no radiation dose, wide field of view, and unlimited penetration depth, there are a few drawbacks. First, the resolution of high-field MRI is still somewhat limited, particularly in the out-of-plane view. We accept that an isotropic resolution would be ideal and work should be done to develop scan techniques with increased out-of-plane resolution while maintaining high levels of tissue contrast. MRI also requires multiple scans which can result in long scan times, especially when high resolution is needed. For ex vivo biomechanics studies, long scan times may be an issue as the tissue cannot be fixed prior to imaging which may lead to tissue degradation over the course of the scans. Additional tissue contrast could be obtained through the use of contrast agents such as gadolinium (Norman et al., 2010), however they may alter the mechanical properties of the eye, and we would hesitate to use them for biomechanics studies until we better understand their effects.

Much work has focused on the development of MRI methods for the study of the eye (Duong et al., 2008; Erb-Eigner et al., 2015; Langner et al., 2010; Lim et al., 2015; Luan et al., 2006; Norman et al., 2010). In an early study, Sawada and colleagues measured changes in axial and equatorial length in rabbit eyes after the injection of mannitol into the vitreous (Sawada et al., 2002). Norman and colleagues measured scleral thickness and axial length in enucleated human eyes (Norman et al., 2010). Several studies have employed MRI to determine axial length and globe shape in both adult and pediatric patients (Erb-Eigner et al., 2015; Lim et al., 2015). MRI techniques are also well suited for studying retinal oxygenation and blood flow (Fan et al., 2015a; Luan et al., 2006). In fact, Luan et al. were able to quantify retinal thickness in rats. Wang and colleagues have recently used MRI to study deformation in the optic nerve during eye movement (Wang et al., 2016) In our previous work, we have used MRI to measure aqueous humor dynamics using gadolinium contrast (Ho et al., 2014a). Additionally, we have used micro-MRI, with in-plane resolution under 30 μm, to examine the collagen microstructure of the optic nerve head and lamina cribrosa using magic angle enhancement (Ho et al., 2014b). More recently, we used a multi-modal MRI approach, consisting of T2-weighted MRI, diffusion tensor MRI and magnetization transfer MRI to study the effects of glycosaminoglycan content and IOP in rat eyes (Ho et al., 2016). This study is the first to demonstrate the use of high-field MRI for measuring whole globe deformations and local deformation of the scleral canal during a controlled inflation test and from a single scan in a large animal model.

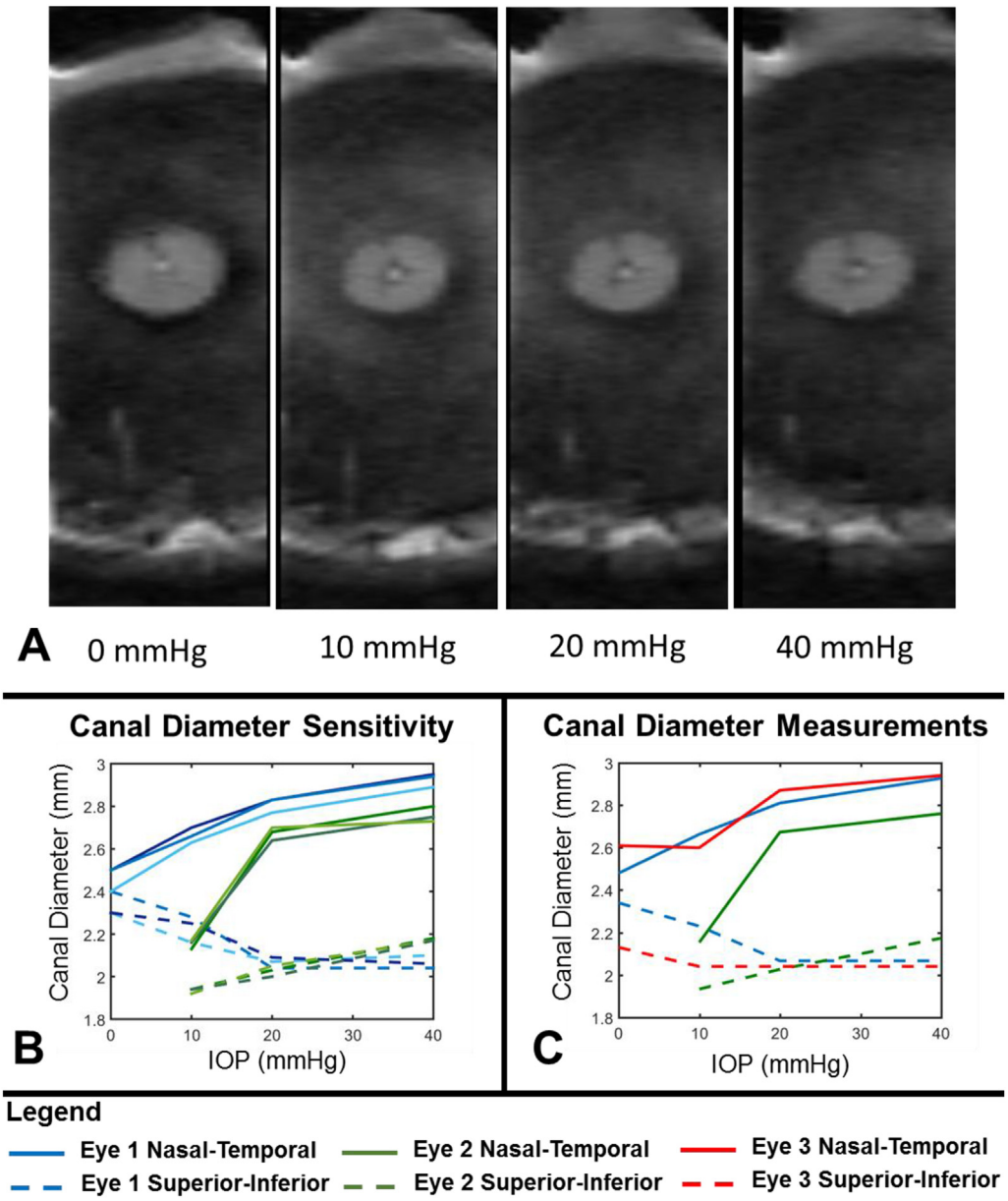

Fig. 9. The scleral canal underwent measurable expansion due to IOP. A. Coronal views showing the scleral canal under 0, 10, 20 and 40 mmHg. The superior-inferior axis is shown top to bottom. B. Measurements of the canal diameters were marked in triplicate to determine measurement sensitivity and the average standard deviation of the triplicate measurements across all eyes, pressures, and axes was 30 μm. C. The nasal-temporal scleral canal diameter (solid lines) increased measurably due to IOP changes. The increase was greatest between IOPs of 10 and 20 mmHg. The superior-inferior canal diameter (dashed lines) only changed measurably in eye 2 (Green dashed line between 10 and 20 mmHg). In eye 2 we could not confidently identify a section at 0 mmHg that could be compared to the other pressures conditions and this condition was not considered in our measurements. Note that the resolution of this scan is higher in the nasal-temporal direction (left-right) than in the superior-inferior direction (top-bottom). Recall that sheep eyes have a scleral canal that is typically more elongated in the nasal-temporal direction than in the superior-inferior one. (For interpretation of the references to colour in this figure legend, the reader is referred to the web version of this article.)

In this study, we measured the diameters of the scleral canal with measurement sensitivity smaller than a voxel. This is possible through the use of sub-voxel resolution image processing and marking. Sub-voxel resolution utilizes local voxel intensity data to interpolate image data. Sub-voxel imaging techniques are valuable tools that can improve image registration and have been commonly employed in computer vision (Bing et al., 2009; Cuevas et al., 2011) and in biomedical research (Nakamura et al., 2008). The high contrast amongst soft tissues in our scans allowed for excellent sub-voxel interpolation. This marking using interpolated images assumed that the inner surfaces of the cornea and sclera are smooth and remain smooth when deformed. If the surfaces were rough or highly contoured, then the interpolation used would become inaccurate. However, the assumption of smoothness is reasonable for the 50 μm scale on which we measured ocular deformations. By utilizing the sub-voxel analysis, we may have enough resolution to calculate local two-dimensional strains across the whole globe and with increased resolution out of the plane it should be feasible to calculate three dimensional strains.

While our study offers a proof of concept for the use of high-field MRI in biomechanics studies, there are limitations to the scope. First, we have only demonstrated the feasibility for conducting ex vivo biomechanics studies. Our scanner is designed for small animal imaging with a small bore, and would not be able to

accommodate a live large animal such as a sheep, but could potentially be used to study small animals with lamina cribrosas, such as marmosets (Shimazawa et al., 2013). However, high-field, 9.4 T clinical MRI systems are becoming more common, meaning that the same measurements we have obtained in this study could potentially be obtained in a large animal in vivo. Additionally, we have only considered a limited number of pressure conditions, and the sensitivity of the technique to detect effects of smaller changes in IOP, particularly in the clinical range between around 15 and 25 mmHg, remains to be determined. It is also important to note that our experimental set-up allows for the free rotation of the eye within the soft gel after IOP change, and we cannot rule out some potential measurement error due to the movement and deformation of landmarks used in image registration. Elsewhere we have demonstrated that 16 × 16 μm in-plane resolution is possible with high-field MRI (Ho et al., 2014b) and in future biomechanical studies the parameters can be further optimized to increase resolution as well as contrast.

In this study, we chose only to measure repeatability with one observer. Our goal was not to investigate the error associated with different observers. Instead we aimed to determine the limits of the technology and the image variability. This includes the interscan variability which can arise from changes in eye-position that may occur when IOP is increased. This variability is partially reflected in the standard deviation measurements we report across all seven eyes.

In summary, we used high-field MRI to measure IOP induced whole-globe deformations including changes in axial length as well as regional deformations such as posterior scleral bowing and scleral canal expansion. We found that increasing IOP results in increases in axial length but not equatorial diameter, suggesting that clamping of the equatorial sclera for half-globe inflation tests and computational modeling is a reasonable assumption. High-field MRI is a powerful new tool for studying ocular biomechanics.

Proprietary interest

None.

Funding

Supported in part by National Institutes of Health R01-EY023966, R01-EY025011, R01-EY013178, P30-EY008098 and T32-EY017271 (Bethesda, MD), BrightFocus Foundation G2013077 (Clarksburg, Maryland), Stimulating Pittsburgh Research in Geroscience Pilot Project Program Award (Pittsburgh, PA) and the Eye and Ear Foundation (Pittsburgh, PA).

Appendix A. Supplementary data

Supplementary data related to this article can be found at http://dx.doi.org/10.1016/j.exer.2017.05.004.

References

Albon, J., Purslow, P.P., Karwatowski, W.S., Easty, D.L., 2000. Age related compliance of the lamina cribrosa in human eyes. Br. J. Ophthalmol. 84, 318–323.
Bajwa, A., Aman, R., Reddy, A.K., 2015. A comprehensive review of diagnostic imaging technologies to evaluate the retina and the optic disk. Int. Ophthalmol. 35, 733–755.
Bellezza, A.J., Rintalan, C.J., Thompson, H.W., Downs, J.C., Hart, R.T., Burgoyne, C.F., 2003a. Anterior scleral canal geometry in pressurised (IOP 10) and non-pressurised (IOP 0) normal monkey eyes. Br. J. Ophthalmol. 87, 1284–1290.
Bellezza, A.J., Rintalan, C.J., Thompson, H.W., Downs, J.C., Hart, R.T., Burgoyne, C.F., 2003b. Deformation of the lamina cribrosa and anterior scleral canal wall in early experimental glaucoma. Invest. Ophthalmol. Vis. Sci. 44, 623–637.
Bing, P., Kemao, Q., Huimin, X., Anand, A., 2009. Two-dimensional digital image correlation for in-plane displacement and strain measurement: a review. Meas. Sci. Technol. 20, 062001.
Brown, H.D.H., Woodall, R.L., Kitching, R.E., Baseler, H.A., Morland, A.B., 2016. Using magnetic resonance imaging to assess visual deficits: a review. Ophthalmic Physiological Opt. 36, 240–265.
Campbell, I.C., Coudrillier, B., Mensah, J., Abel, R.L., Ethier, C.R., 2015. Automated segmentation of the lamina cribrosa using Frangi's filter: a novel approach for rapid identification of tissue volume fraction and beam orientation in a trabeculated structure in the eye. J. R. Soc. Interface 12, 20141009.
Coudrillier, B., Boote, C., Quigley, H.a., Nguyen, T.D., 2013. Scleral anisotropy and its effects on the mechanical response of the optic nerve head. Biomech. Model Mechanobiol. 12, 941–963.
Coudrillier, B., Geraldes, D.M., Vo, N.T., Atwood, R., Reinhard, C., Campbell, I.C., Raji, Y., Albon, J., Abel, R.L., Ethier, C.R., 2016. Phase-contrast micro-computed tomography measurements of the intraocular pressure-induced deformation of the porcine lamina cribrosa. IEEE Trans. Med. Imaging 35, 988–999.
Coudrillier, B., Pijanka, J.K., Jefferys, J., Sorensen, T., Quigley, H.A., Boote, C., Nguyen, T.D., 2015. Effects of age and diabetes on scleral stiffness. J. biomechanical Eng. 137 (7), 071007.
Cruz Perez, B., Pavlatos, E., Morris, H.J., Chen, H., Pan, X., Hart, R.T., Liu, J., 2016. Mapping 3D strains with ultrasound speckle tracking: method validation and initial results in porcine scleral inflation. Ann. Biomed. Eng. 44, 2302–2312.
Cuevas, E., Zaldivar, D., Perez-Cisneros, M., Ramirez-Ortegon, M., 2011. Circle detection using discrete differential evolution optimization. Pattern Analysis Appl. 14, 93–107.
Dai, C., Zhou, C., Fan, S., Chen, Z., Chai, X., Ren, Q., Jiao, S., 2012. Optical coherence tomography for whole eye segment imaging. Opt. express 20, 6109–6115.
Deol, M., Taylor, D.A., Radcliffe, N.M., 2015. Corneal hysteresis and its relevance to glaucoma. Curr. Opin. Ophthalmol. 26, 96–102.
Duong, T.Q., Pardue, M.T., Thule, P.M., Olson, D.E., Cheng, H., Nair, G., Li, Y., Kim, M., Zhang, X., Shen, Q., 2008. Layer-specific anatomical, physiological and functional MRI of the retina. NMR Biomed. 21, 978–996.
Erb-Eigner, K., Hirnschall, N., Hackl, C., Schmidt, C., Asbach, P., Findl, O., 2015. Predicting lens diameter: ocular biometry with high-resolution MRI. Invest. Ophthalmol. Vis. Sci. 56, 6847–6854.
Ethier, C.R., Johnson, M., Ruberti, J., 2004. Ocular biomechanics and biotransport. Annu. Rev. Biomed. Eng. 6, 249–273.
Fan, N., Wang, P., Tang, L., Liu, X., 2015a. Ocular blood flow and normal tension glaucoma. BioMed Res. Int. 2015, 308505.
Fan, S., Li, L., Li, Q., Dai, C., Ren, Q., Jiao, S., Zhou, C., 2015b. Dual band dual focus optical coherence tomography for imaging the whole eye segment. Biomed. Opt. Express 6, 2481–2493.
Fortune, B., 2015. In vivo imaging methods to assess glaucomatous optic neuropathy. Exp. eye Res. 141, 139–153.
Girard, M.J.a., Downs, J.C., Burgoyne, C.F., Suh, J.-K.F., 2009. Peripapillary and posterior scleral mechanics–part I: development of an anisotropic hyperelastic constitutive model. J. biomechanical Eng. 131, 051011.
Grytz, R., Fazio, M.A., Libertiaux, V., Bruno, L., Gardiner, S., Girkin, C.A., Downs, J.C., 2014. Age- and race-related differences in human scleral material properties. Invest. Ophthalmol. Vis. Sci. 55, 8163–8172.
Hann, C.R., Bentley, M.D., Vercnocke, A., Ritman, E.L., Fautsch, M.P., 2011. Imaging the aqueous humor outflow pathway in human eyes by three-dimensional micro-computed tomography (3D micro-CT). Exp. eye Res. 92, 104–111.
He, X., Liu, J., 2009. A quantitative ultrasonic spectroscopy method for noninvasive determination of corneal biomechanical properties. Invest. Ophthalmol. Vis. Sci. 50, 5148–5154.
Ho, L.C., Conner, I.P., Do, C.-W., Kim, S.-G., Wu, E.X., Wollstein, G., Schuman, J.S., Chan, K.C., 2014a. In vivo assessment of aqueous humor dynamics upon chronic ocular hypertension and hypotensive drug treatment using gadolinium-enhanced MRI. Investigative Ophthalmol. Vis. Sci. 55, 3747–3757.
Ho, L.C., Sigal, I.A., Jan, N.-J., Yang, X., van der Merwe, Y., Yu, Y., Chau, Y., Leung, C.K., Conner, I.P., Jin, T., Wu, E.X., Kim, S.-G., Wollstein, G., Schuman, J.S., Chan, K.C., 2016. Non-invasive MRI assessments of tissue microstructures and macromolecules in the eye upon biomechanical or biochemical modulation. Sci. Rep. 6, 32080.
Ho, L.C., Sigal, I.A., Jan, N.J., Squires, A., Tse, Z., Wu, E.X., Kim, S.G., Schuman, J.S., Chan, K.C., 2014b. Magic angle-enhanced MRI of fibrous microstructures in sclera and cornea with and without intraocular pressure loading. Invest. Ophthalmol. Vis. Sci. 55, 5662–5672.
Jan, N.-J., Grimm, J.L., Tran, H., Lathrop, K.L., Wollstein, G., Bilonick, R.A., Ishikawa, H., Kagemann, L., Schuman, J.S., Sigal, I.A., 2015. Polarization microscopy for characterizing fiber orientation of ocular tissues. Biomed. Opt. Express 6, 4705–4718.
Jonas, J.B., Holbach, L., 2005. Central corneal thickness and thickness of the lamina cribrosa in human eyes. Invest. Ophthalmol. Vis. Sci. 46, 1275–1279.
Kilker, B.A., Holst, J.M., Hoffmann, B., 2014. Bedside ocular ultrasound in the emergency department. Eur. J. Emerg. Med. official J. Eur. Soc. Emerg. Med. 21, 246–253.
Kostanyan, T., Wollstein, G., Schuman, J.S., 2015. New developments in optical coherence tomography. Curr. Opin. Ophthalmol. 26, 110–115.
Langner, S., Martin, H., Terwee, T., Koopmans, S.A., Kruger, P.C., Hosten, N., Schmitz, K.P., Guthoff, R.F., Stachs, O., 2010. 7.1 T MRI to assess the anterior segment of the eye. Invest. Ophthalmol. Vis. Sci. 51, 6575–6581.
Lim, L.S., Chua, S., Tan, P.T., Cai, S., Chong, Y.S., Kwek, K., Gluckman, P.D., Fortier, M.V., Ngo, C., Qiu, A., Saw, S.M., 2015. Eye size and shape in newborn children and their relation to axial length and refraction at 3 years. Ophthalmic &

physiological Opt. J. Br. Coll. Ophthalmic Opt. (Optometrists) 35, 414–423.
Lorente-Ramos, R.M., Arman, J.A., Munoz-Hernandez, A., Gomez, J.M., de la Torre, S.B., 2012. US of the eye made easy: a comprehensive how-to review with ophthalmoscopic correlation. Radiogr. a Rev. Publ. Radiological Soc. N. Am. Inc 32, E175–E200.
Luan, H., Roberts, R., Sniegowski, M., Goebel, D.J., Berkowitz, B.A., 2006. Retinal thickness and subnormal retinal oxygenation response in experimental diabetic retinopathy. Investigative Ophthalmol. Vis. Sci. 47, 320–328.
Malhotra, A., Minja, F.J., Crum, A., Burrowes, D., 2011. Ocular anatomy and cross-sectional imaging of the eye. Seminars ultrasound, CT, MR 32, 2–13.
Medeiros, F.A., Freitas, D., Lisboa, R., Kuang, T.-M., Zangwill, L.M., Weinreb, R.N., 2013. Corneal hysteresis as a risk factor for glaucoma progression: a prospective longitudinal study. Ophthalmology 120, 1533–1540.
Nakamura, M., Wada, S., Miki, T., Shimada, Y., Suda, Y., Tamura, G., 2008. Automated segmentation and morphometric analysis of the human airway tree from multidetector CT images. The journal of physiological sciences: JPS 58, 493–498.
Norman, R.E., Flanagan, J.G., Rausch, S.M., Sigal, I.A., Tertinegg, I., Eilaghi, A., Portnoy, S., Sled, J.G., Ethier, C.R., 2010. Dimensions of the human sclera: thickness measurement and regional changes with axial length. Exp. eye Res. 90, 277–284.
Palko, J.R., Morris, H.J., Pan, X., Harman, C.D., Koehl, K.L., Gelatt, K.N., Plummer, C.E., Komaromy, A.M., Liu, J., 2016. Influence of age on ocular biomechanical properties in a canine glaucoma model with ADAMTS10 mutation. PLoS One 11, e0156466.
Pijanka, J.K., Abass, A., Sorensen, T., Elsheikh, A., Boote, C., 2013. A wide-angle X-ray fibre diffraction method for quantifying collagen orientation across large tissue areas: application to the human eyeball coat. J. Appl. Crystallogr. 46, 1481–1489.
Sawada, T., Nakamura, J., Nishida, Y., Kani, K., Morikawa, S., Inubushi, T., 2002. Magnetic resonance imaging studies of the volume of the rabbit eye with intravenous mannitol. Curr. Eye Res. 25, 173–177.
Schindelin, J., Arganda-Carreras, I., Frise, E., Kaynig, V., Longair, M., Pietzsch, T., Preibisch, S., Rueden, C., Saalfeld, S., Schmid, B., Tinevez, J.Y., White, D.J., Hartenstein, V., Eliceiri, K., Tomancak, P., Cardona, A., 2012. Fiji: an open-source platform for biological-image analysis. Nat. methods 9, 676–682.
Shimazawa, M., Nakamura, S., Miwa, M., Tsuruma, K., Aihara, M., Nakamura, K., Hara, H., 2013. Establishment of the ocular hypertension model using the common marmoset. Exp. eye Res. 111, 1–8.
Sigal, I.A., Ethier, C.R., 2009. Biomechanics of the optic nerve head. Exp. eye Res. 799–807.
Sigal, I.A., Flanagan, J.G., Tertinegg, I., Ethier, C.R., 2005. Reconstruction of human optic nerve heads for finite element modeling. Technol. health care official J. Eur. Soc. Eng. Med. 13, 313–329.
Sigal, I.A., Wang, B., Strouthidis, N.G., Akagi, T., Girard, M.J., 2014. Recent advances in OCT imaging of the lamina cribrosa. Br. J. Ophthalmol. 98 (Suppl. 2), ii34–39.
Strouthidis, N.G., Fortune, B., Yang, H., Sigal, I.A., Burgoyne, C.F., 2011. Effect of acute intraocular pressure elevation on the monkey optic nerve head as detected by spectral domain optical coherence tomography. Investigative Ophthalmol. Vis. Sci. 52, 9431–9437.
Tran, H., Wang, Y., Wang, B., Wollstein, G., Smith, M.A., Kagemann, L., Ishikawa, H., Schuman, J.S., Tyler-Kabara, E., Sigal, I.A., 2015. In-vivo laminar and scleral canal displacements during acute intracranial and intraocular pressure elevation in monkeys. Investigative Ophthalmol. Vis. Sci. 56, 6150.
Wang, B., Sigal, I.A., Smith, M.A., Kostanyan, T., Bilonick, R.A., Tran, H., Kagemann, L., Tyler-Kabara, E., Schuman, J.S., Wollstein, G., 2015. In-vivo 3D deformation of lamina cribrosa microstructure in response to acute changes in intraocular and cerebrospinal fluid pressures. Investigative Ophthalmol. Vis. Sci. 56, 3979.
Wang, X., Rumpel, H., Lim, W.E., Baskaran, M., Perera, S.A., Nongpiur, M.E., Aung, T., Milea, D., Girard, M.J., 2016. Finite element analysis predicts large optic nerve head strains during horizontal eye movements. Invest. Ophthalmol. Vis. Sci. 57, 2452–2462.
Whitford, C., Joda, A., Jones, S., Bao, F., Rama, P., Elsheikh, A., 2016. Ex vivo testing of intact eye globes under inflation conditions to determine regional variation of mechanical stiffness. Eye Vis. Lond. Engl. 3, 21.
Yan, D.B., Coloma, F.M., Metheetrairut, A., Trope, G.E., Heathcote, J.G., Ethier, C.R., 1994. Deformation of the lamina cribrosa by elevated intraocular pressure. Br. J. Ophthalmol. 78, 643–648.